Cerium Valence Change in the Solid Solutions $Ce(Rh_{1-x}Ru_x)Sn$

Oliver Niehaus[a], Paula M. Abdala[b], Jan F. Riecken[a], Florian Winter[a], Bernard Chevalier[c], and Rainer Pöttgen[a]

[a] Institut für Anorganische und Analytische Chemie and NRW Graduate School of Chemistry, Universität Münster, Corrensstraße 30, D-48149 Münster, Germany

[b] SNBL at ESRF, European Synchrotron Radiation Facility, 6 Rue Jules Horowitz, BP 220, Grenoble, France

[c] CNRS, Université de Bordeaux, ICMCB, 87 Avenue du Dr. A. Schweitzer, 33608 Pessac-Cedex, France

Reprint requests to R. Pöttgen. E-mail: pottgen@uni-muenster.de

Z. Naturforsch. **2013**, *68b*, 960 – 970 / DOI: 10.5560/ZNB.2013-3176
Received July 1, 2013

The solid solutions $Ce(Rh_{1-x}Ru_x)Sn$ were investigated by means of susceptibility measurements, specific heat, electrical resistivity, X-ray absorption spectroscopy (XAS), and ^{119}Sn Mössbauer spectroscopy. Magnetic measurements as well as XAS data show a cerium valence change in dependence on the ruthenium content. Higher ruthenium content causes an increase from 3.22 to 3.45 at 300 K. Furthermore χ and χ^{-1} data indicate valence fluctuation for cerium as a function of temperature. For example, $Ce(Rh_{0.8}Ru_{0.2})Sn$ exhibits valence fluctuations between 3.42 and 3.32 in the temperature range of 10 to 300 K. This could be proven by using the interconfiguration fluctuation (ICF) model introduced by Sales and Wohlleben. Cerium valence change does not influence the tin atoms as proven by ^{119}Sn Mössbauer spectroscopy, but it influences the electrical properties. $Ce(Rh_{0.9}Ru_{0.1})Sn$ behaves like a typical valence fluctuating compound, and higher ruthenium content causes an increase of the metallic behavior.

Key words: Cerium, Intermediate, Valence, Magnetic Properties

Introduction

Cerium intermetallics with equiatomic composition Ce*TX* (*T* = transition metal; *X* = element of the 3rd, 4th, or 5th main group) have intensively been studied in the last forty years with respect to their broadly varying magnetic and electrical properties. Variation of *T* and *X* components leads to changes in structure type and furthermore to a manifold of magnetic ground states. Outstanding examples are intermediate-valent CeNiIn [1] and CeRhSn [2], the 10 K ferromagnet CeAuGe [3], or the 9.3 K antiferromagnet CeRhGe [4]. Changes of the structure and the magnetic ground state can be induced by pressure [5], by hydrogenation [6, 7], or in solid solutions, either by substitution of the *T* or *X* component [8 – 10], influencing the cerium 4*f* states. Most of the Ce*TX* intermetallics crystallize with the hexagonal ZrNiAl-type structure or with one of the many superstructure variants of the hexagonal AlB_2 type [11].

A prominent example with a unique crystal structure in the Ce*TX* family is CeRuSn [12 – 19]. This ternary stannide belongs to a larger class of compounds with extremely short Ce–Ru distances [20, 21] which are a consequence of almost tetravalent cerium. CeRuSn crystallizes with a commensurate superstructure of the monoclinic CeCoAl type and adopts complex modulations at lower temperature. Just below room temperature the changes in crystal structure are associated with large thermal hysteretic effects in the magnetic susceptibility, in the specific heat, as well as in electronic and heat transport properties. The trivalent cerium atoms show long-range antiferromagnetic ordering below $T_N = 2.7$ K [14]. So far, only CeCoAl and CeCoGa [22], with the same valence electron count, adopt monoclinic structures similar to CeRuSn.

We have now initiated systematic studies of solid solutions starting from CeRuSn. Since the CeRuSn structure contains one pronounced site for trivalent and a second one for tetravalent cerium, one possibility is

partial substitution of trivalent cerium by diamagnetic La^{3+} [23]. On the other hand it is possible to substitute the transition metal and *p*-element site which results in an electronic influence on the polyanionic network. Herein we present the complete set of solid solutions $Ce(Rh_{1-x}Ru_x)Sn$. Our substitution experiments have shown that the CeRuSn structure tolerates only tiny amounts of rhodium and a rapid switch to the hexagonal ZrNiAl-type structure of CeRhSn [2, 24]. Echizen *et al.* investigated this solid solution up to a ruthenium content of $x = 0.25$ [25].

Experimental

Synthesis

Starting materials for the syntheses of all samples were a cerium ingot (Sigma Aldrich), ruthenium and rhodium powder (Allgemeine Pforzheim), and tin granules (Merck), all with a stated purity better than 99.9 %. Pieces of the cerium ingot were first arc-melted into small buttons under purified argon [26]. The argon was purified over molecular sieves, silica gel and a titanium sponge (900 K). The elements were weighed in the ideal stoichiometric ratio (the ruthenium and rhodium powder were cold-pressed to pellets of 6 mm diameter) and arc-melted under an argon pressure of *ca*. 800 mbar. The molten buttons were remelted three times to ensure homogeneity. Samples of the solid solution are stable in air over months.

Powder X-ray data

The polycrystalline samples were characterized by Guinier powder patterns (imaging plate technique, Fujifilm BAS-1800) using Cu$K_{\alpha 1}$ radiation and α-quartz ($a = 491.30$ and $c = 540.46$ pm) as an internal standard. Standard least-squares refinements led to the lattice parameters listed in Table 1. Comparison of the experimental patterns with calculated ones assured correct indexing [12, 27].

Physical property measurements

The magnetic susceptibility and heat capacity measurements were carried out on a Quantum Design Physical Property Measurement System (PPMS) using the Vibrating Sample Magnetometer (VSM) option, respectively the Heat Capacity (HC) option. For the measurements, approximately 20 mg of the powdered samples were packed in a polypropylene capsule and attached to the sample holder rod. For the heat capacity measurements, pieces of the samples (about 20 mg) were fixed to a pre-calibrated heat capacity puck using Apiezon N grease. Magnetic investigations were performed in the temperature range of 2.5 to 305 K with magnetic flux densities up to 80 kOe and heat capacity measurements in the temperature range of 2.1 to 305 K ($1\ \text{kOe} = 7.96 \times 10^4\ \text{A m}^{-1}$).

The measurements of the electrical resistivity were carried out above 4.2 K on a bar of $0.5 \times 0.5 \times 3\ \text{mm}^3$ using a standard dc four probe method with silver paint contacts and an intensity current of 10 mA.

XANES – X-ray absorption near edge structure

X-Ray absorption spectra at the CeL_{III} edge were collected at BM01B (Swiss Norwegian Beamlines, SNBL) at the European Synchrotron Radiation Facility (ESRF), Grenoble, France. The electron energy in the storage ring was 6 GeV with a maximum current of 200 mA. The measurements were performed in transmission mode using a Si(111) double crystal monochromator. The second crystal of the monochromator was detuned by 60 % in order to suppress higher harmonic radiation. The intensities of the incident

Table 1. Lattice parameters of different samples of the solid solutions $Ce(Rh_{1-x}Ru_x)Sn$.

Compound	a (pm)	b (pm)	c (pm)	β (deg)	V (nm^3)	Reference
CeRhSn	744.8	–	408	–	0.1960	[41]
$Ce(Rh_{0.9}Ru_{0.1})Sn$	743.8(1)	–	407.9(1)	–	0.1954	this work
$Ce(Rh_{0.8}Ru_{0.2})Sn$	743.6(1)	–	407.8(1)	–	0.1953	this work
$Ce(Rh_{0.7}Ru_{0.3})Sn$	742.8(1)	–	407.7(1)	–	0.1948	this work
$Ce(Rh_{0.6}Ru_{0.4})Sn$	742.4(2)	–	407.8(1)	–	0.1946	this work
$Ce(Rh_{0.5}Ru_{0.5})Sn$	741.9(1)	–	407.7(1)	–	0.1943	this work
$Ce(Rh_{0.4}Ru_{0.6})Sn$	741.2(1)	–	407.8(1)	–	0.1940	this work
$Ce(Rh_{0.3}Ru_{0.7})Sn$	740.5(1)	–	407.7(1)	–	0.1936	this work
$Ce(Rh_{0.25}Ru_{0.75})Sn$	740.4(1)	–	407.8(1)	–	0.1937	this work
$Ce(Rh_{0.2}Ru_{0.8})Sn$	739.8(1)	–	407.9(1)	–	0.1933	this work
$Ce(Rh_{0.2}Ru_{0.8})Sn$	1156.8(3)	475.4(1)	1022.6(3)	102.81(3)	0.5484	this work
$Ce(Rh_{0.15}Ru_{0.85})Sn$	740.7(1)	–	407.9(1)	–	–	this work
$Ce(Rh_{0.1}Ru_{0.9})Sn$	1155.5(3)	474.7(1)	1023.0(3)	103.04(2)	0.5467	this work
$Ce(Rh_{0.05}Ru_{0.95})Sn$	1155.9(3)	475.4(1)	1022.0(1)	102.92(1)	0.5474	this work
CeRuSn	1155.3(1)	475.0(1)	1023.0(4)	102.96(1)	0.5469	this work
CeRuSn	1156.1(4)	475.9(2)	1023.3(4)	102.89(3)	0.5488	[12]

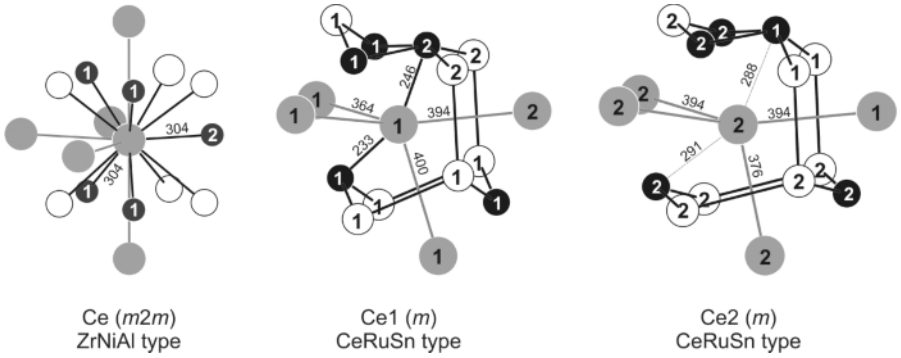

Fig. 1. The near neighbor coordination of cerium in CeRhSn (left) and CeRuSn (middle and right). Cerium, rhodium (ruthenium) and tin atoms are drawn as medium grey, black filled and open circles, respectively. Relevant interatomic distances are indicated.

and transmitted X-rays were monitored with nitrogen- and helium-filled ionization chambers. All spectra were acquired in a continuous scanning mode from 5680 to 6140 eV, with energy steps of 0.3 eV for 15 min each scan.

In order to optimize the edge jump, the powdered samples were homogeneously mixed with small amounts of cellulose and pressed into pellets. Measurements were performed at ambient conditions. Experimental data were recorded in $Ce_2(CO_3)_3$ or CeO_2 as reference compounds with Ce ions in a trivalent and tetravalent state, respectively.

^{119}Sn Mössbauer spectroscopy

The ^{119}Sn Mössbauer spectroscopic experiments were performed in the usual transmission geometry in a commercial cryostat, using the 23.87 keV transition of ^{119}Sn. The temperature of the absorber could be varied between 78 K and room temperature. A $Ca^{119m}SnO_3$ source was used for the ^{119}Sn Mössbauer spectroscopic investigation and kept at room temperature. To reduce the Sn*K* X-rays concurrently emitted by this source, a palladium foil of 0.05 mm thickness was used. The sample was ground under *n*-hexane and placed within a thin-walled PMMA container at a thickness corresponding to about 10 mg Sn cm^{-2}.

Results and Discussion

Crystal chemistry

The crystal structures of CeRuSn and CeRhSn have been discussed in previous papers [2, 12 – 19, 24, 27, and references therein]. We give only a short description here. As mentioned above, CeRuSn crystallizes with a superstructure of the monoclinic CeCoAl type and contains two cerium sites. One contains only trivalent cerium whereas the other shows intermediate valence behavior. This can be described by the coordination spheres (Fig. 1) that contain four cerium, five ruthenium and seven tin atoms. Both cerium sites show the same topology, however, small distortions result in significantly different interatomic distances. The Ce1–Ru distances of 233 and 246 pm are drastically shorter than the sum of the covalent radii (289 pm) [28]. The Ce2–Ru distances amount to 288 and 291 pm. CeRhSn has only one independent cerium site with a coordination number of 15 (pentacapped pentagonal prism) with four cerium, five rhodium and six tin atoms in the coordination sphere (Fig. 1). Relatively short Ce–Rh distances of 304 pm can be observed in this structure. This value is between the sums of the covalent and intermetallic radii of 290 and 317 pm [28], respectively. The striking structural features in both ternary stannides are short cerium-transition metal distances, indicating strong bonding between these elements.

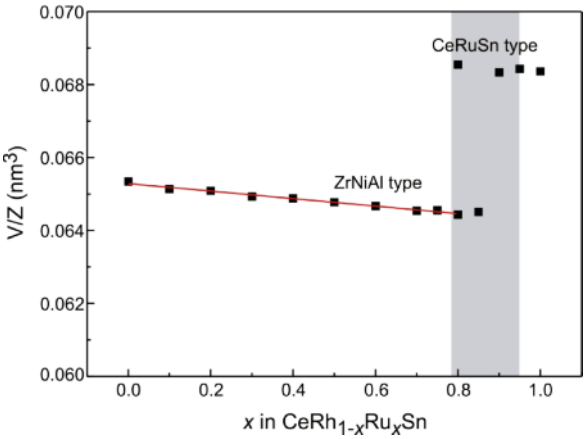

Fig. 2 (color online). Behavior of the unit cell volume of the solid solutions $Ce(Rh_{1-x}Ru_x)Sn$ as a function of the ruthenium content. The development of the unit cell volumina with ZrNiAl-type structure is presented by a line of the best fit (red) and conforms with Vegard's law.

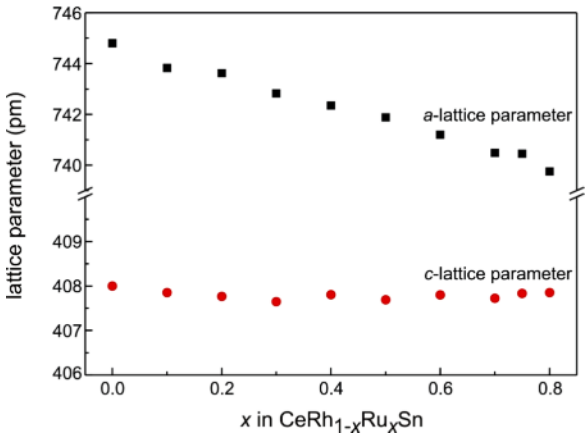

Fig. 3 (color online). Development of the a and c lattice parameters of the solid solutions $Ce(Rh_{1-x}Ru_x)Sn$ with ZrNiAl-type structure.

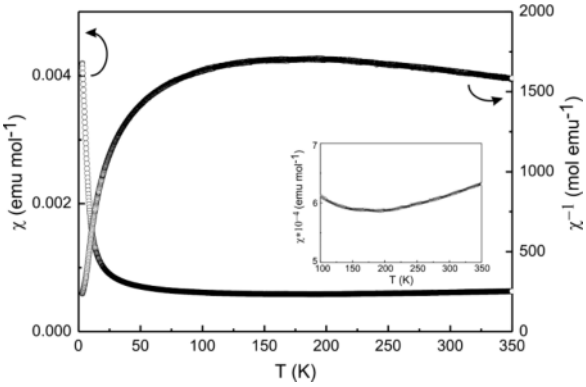

Fig. 4. Temperature dependence of the magnetic susceptibility χ and its reciprocal χ^{-1} of $Ce(Rh_{0.25}Ru_{0.75})Sn$ measured with a magnetic field of 10 kOe. The inset shows the magnified susceptibility χ in the temperature area between 100 and 350 K.

All samples of the solid solution concerned crystallize up to a ruthenium content of $x = 0.75$ in the ZrNiAl-type structure ($P\bar{6}2m$) similar to CeRhSn. Higher ruthenium content leads to a mixture of the hexagonal phase and a monoclinic phase (CeRuSn-type structure, $C2/m$). The two-phase area exists between $x \approx 0.78$ and 0.95. The development of the unit cell volume in dependence of the ruthenium content conforms to Vegard's law for $x < 0.8$ (Fig. 2). In the two-phase area no further decrease of the unit cell volume can be observed for both structure types. SEM/EDX investigations confirm these results since only tiny amounts of rhodium can be detected in the samples with CeRuSn-type structure.

Fig. 3 displays the development of the lattice parameters of $Ce(Rh_{1-x}Ru_x)Sn$ with ZrNiAl-type structure. The a parameter is decreasing with higher ruthenium content, while the c parameter remains constant in the whole area. This can be explained by the features of this structure type. The short Ce–Rh/Ru distance is placed in direction of the a axis. Accordingly, the interactions between these atoms become stronger with higher ruthenium content.

Magnetic measurements

Fig. 4 displays the temperature dependence of the magnetic susceptibility and its reciprocal (χ and χ^{-1} data) of $Ce(Rh_{0.25}Ru_{0.75})Sn$ measured with a magnetic field of 10 kOe. Exceptional increase of χ can be observed in the temperature range from 200 to 350 K, leading to a characteristic broad maximum at higher temperature that is typical for valence-fluctuating compounds, as is the small value of χ (in the order of 10^{-3} emu mol^{-1} Ce atom) [29]. The increase of χ above 200 K can only be explained by a higher amount of trivalent cerium at higher temperatures. However, at low temperatures, χ increases instead of tending to a constant value as could be expected for tetravalent cerium. Consequently, at low temperatures both cerium valence states (Ce^{3+} and Ce^{4+}) are occupied. Such a low-temperature tail in $\chi(T)$ is frequently observed for valence-fluctuating cerium-based compounds and is explained by small additional amounts of Ce^{3+}-containing impurities [29, and references therein]. The contribution to the low-temperature tail in $\chi(T)$ is discussed in detail later.

Sales and Wohlleben developed a model (*i*nter*c*onfiguration *f*luctuation model, ICF) addressing this behavior [30]. We give only a brief introduction to this well described model [29 – 32, and references therein]. The model assumes two distinct states of the rare earth atom, and each is characterized by a different occupation of the $4f$ shell. Eq. 1 shows that the overall magnetic susceptibility can be described by the sum of three different parts, a valence fluctuation part, a part for stable Ce^{3+} (including the trace amounts of possible impurities) and a temperature independent part. Eq. 2 displays a pseudo-Boltzmann statistic that is used to describe

Compound	E_{ex}/k_B (K)	T_{sf} (K)	n	χ_0 (emu mol^{-1})	Valence at 300 K
$Ce(Rh_{0.9}Ru_{0.1})Sn$	565(1)	575(3)	0.0222(1)	4.6(1)E^{-04}	3.24
$Ce(Rh_{0.8}Ru_{0.2})Sn$	960(5)	644(4)	0.0273(1)	5.2(1)E^{-04}	3.32
$Ce(Rh_{0.7}Ru_{0.3})Sn$	2650(7)	1397(4)	0.0140*	7.7E^{-04}*	3.44
$Ce(Rh_{0.6}Ru_{0.4})Sn$	1925(4)	995(2)	0.0232*	6.4E^{-04}*	3.42
$Ce(Rh_{0.5}Ru_{0.5})Sn$	2040(2)	1060(1)	0.0187*	5.8E^{-04}*	3.43
$Ce(Rh_{0.4}Ru_{0.6})Sn$	3391(16)	1779(10)	0.0179*	7.0E^{-04}*	3.46
$Ce(Rh_{0.3}Ru_{0.7})Sn$	2479(7)	1295(5)	0.0222*	5.3E^{-04}*	3.44
$Ce(Rh_{0.25}Ru_{0.75})Sn$	2718(5)	1422(3)	0.0154*	4.8E^{-04}*	3.45

Table 2. Fitting parameters of the magnetic measurements (χ^{-1} data) with the Sales-Wohlleben model. Parameters marked with an asterisk were calculated with a modified Curie-Weiss law and kept fixed during the fitting procedure.

the interconfiguration fluctuations.

$$\chi(T) = \left(\frac{N}{3k_B}\right)\left[\frac{\mu_1^2 \nu(T) + \mu_2^2(1-\nu(T))}{T+T_{sf}}\right] + n\left(\frac{C}{T}\right) + \chi_0 \quad (1)$$

$$\nu(T) = \frac{2J_1+1}{(2J_1+1)+(2J_2+1)\exp\left(\frac{-E_{ex}}{k_B(T+T_{sf})}\right)} \quad (2)$$

In these expressions: (i) $E_{ex} = E(Ce^{3+}) - E(Ce^{4+})$ is the energy gap between the ground states of each cerium configuration; (ii) T_{sf} the quantum spin fluctuation temperature; (iii) $\nu(T)$ the fractional occupancy of the Ce^{4+} state (valence $= 3 + \nu(T)$); (iv) J_1, J_2, μ_1 and μ_2, respectively, the quantum numbers and effective magnetic moments corresponding to the two levels ($J_1 = \mu_1 = 0$ for Ce^{4+}; $J_2 = 5/2$ and $\mu_2 = 2.54\,\mu_B$ for Ce^{3+}); (v) n the proportion of stable Ce^{3+} ($C = 0.807$ emu K mol^{-1}) in the impurity, and (vi) χ_0 the temperature-independent part of magnetism.

Table 2 presents the fitting parameters using the ICF model. To prevent over-determination it was necessary to fix the temperature independent part χ_0 and the amount of stable Ce^{3+} n in some cases. To achieve valuable starting parameters, at first a fit with a modified Curie-Weiss law (Eq. 3) was performed in the range of the low-temperature tail (including the Ce^{3+} contributions from trace impurities).

$$\chi_{mol} = \frac{C}{T-\Theta} + \chi_0 \quad (3)$$

Susceptibility measurements using an applied magnetic field of 10 kOe have been performed for all compounds of the solid solutions $Ce(Rh_{1-x}Ru_x)Sn$ with ZrNiAl-type structure. In Fig. 5 the temperature dependence of the reciprocal magnetic susceptibility (χ^{-1}) is displayed. Striking feature is the non-linear behavior of χ^{-1} for all samples indicating valence fluctuations. Results of the fitting procedure using the ICF model prove this estimation and indicate an increase of the cerium valence with higher ruthenium contents (Table 2). Cerium valences at different temperatures can be calculated by Eq. 2 using the fitting parameters. The development of the cerium valence in dependence of the temperature is shown in Fig. 6. It clearly indicates a maximum of the valence fluctuations in the range of $0.2 \le x \le 0.3$ and the increase of the cerium valence with higher ruthenium contents up to $x = 0.3$. Above $x = 0.4$ the cerium valence remains almost constant. All fitting parameters and calculated cerium valences clearly indicate that trace impurities as well as a partially occupied Ce^{3+} state contribute to the low-temperature tail in $\chi(T)$. Fitting the susceptibility data with the ICF model therefore proves the cerium valence change in dependence of the ruthenium content and temperature. Valence fluctuations in cerium compounds are also known for Ce_2Ni_2In, Ce_2Rh_2In [29], $CeIr_2Si_2$ [31] and have already been proven by Ślebarski *et al.* for CeRhSn [32].

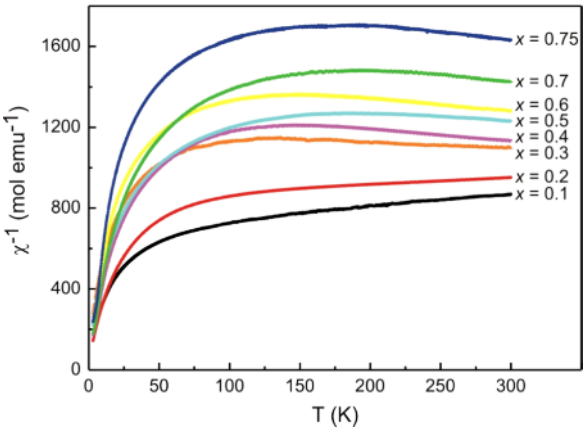

Fig. 5 (color online). Temperature dependence of the reciprocal magnetic susceptibility χ^{-1} of $Ce(Rh_{1-x}Ru_x)Sn$ with $0.1 \le x \le 0.75$ measured with a magnetic field of 10 kOe.

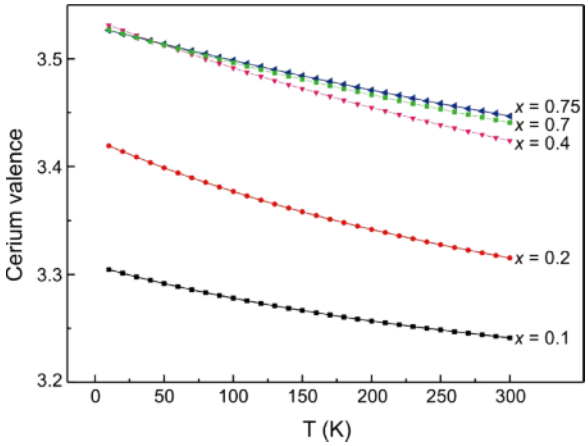

Fig. 6 (color online). Calculated cerium valence for some Ce($Rh_{1-x}Ru_x$)Sn compounds in the temperature range from 5 to 300 K applying the ICF model [30].

Heat capacity

Fig. 7 presents heat capacity measurements of Ce($Rh_{0.9}Ru_{0.1}$)Sn and Ce($Rh_{0.25}Ru_{0.75}$)Sn. The high-temperature specific heat data are quite similar for all investigated samples. At about 5.5 K a λ-shaped anomaly can be observed for both compounds. Especially Ce($Rh_{0.9}Ru_{0.1}$)Sn shows a well pronounced one. This anomaly was also reported by Ślebarski *et al.* [32]. Their investigations led to the result that only a small fraction of the sample is responsible for this transition. This result is in good agreement with a publication by Öner *et al.* [33]. They reported also a small λ-shaped anomaly at 5.5 K in $CeNi_2Sn$ arising from a minor Ce_2O_3 impurity. The thermodynamic investigations on Ce_2O_3 have been performed by Huntelaar *et al.* [34]. A minor Ce_2O_3 phase could also describe the small amount of stable Ce^{3+} determined by fitting the susceptibility data with the ICF model. We have fitted both heat capacity plots between 7.5 and 25 K to the expression $C(T) = \gamma T + \beta T^3$. The first term presents the electronic, the second the phonon contribution to the specific heat. We determined the values $\gamma = 28(2)$ mJ mol^{-1} K^{-2} and $\beta = 0.53(1)$ mJ mol^{-1} K^{-4} for $CeRh_{0.9}Ru_{0.1}Sn$ and $\gamma = 18(3)$ mJ mol^{-1} K^{-2} and $\beta = 0.55(1)$ mJ mol^{-1} K^{-4} for $CeRh_{0.25}Ru_{0.75}Sn$. The coefficient β gives Debye temperatures of $\Theta_D = 222$ and 220 K in the low-temperature area. This value was calculated by the expression $\beta = (12/5)\pi^4 NR(1/\Theta_D)^3$, where N is the number of atoms per formula unit and R is the ideal gas constant. The γ and Θ_D values are in the typical range observed for valence fluctuating cerium intermetallics. Some examples are summarized in [35].

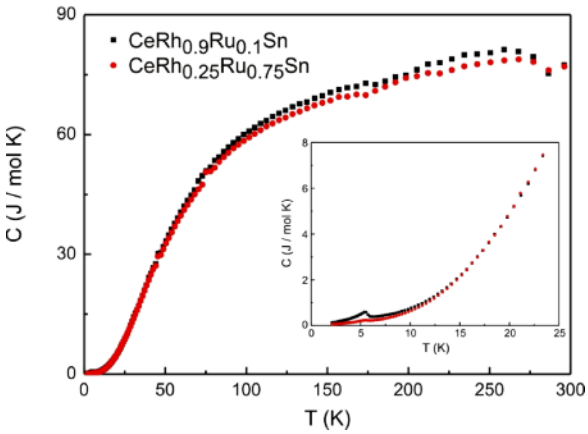

Fig. 7 (color online). Heat capacity of Ce($Rh_{0.9}Ru_{0.1}$)Sn and Ce($Rh_{0.25}Ru_{0.75}$)Sn measured in the temperature range of 2.1 to 305 K. The inset shows the magnified low-temperature area. The anomaly at 5.5 K is most likely due to a minor Ce_2O_3 impurity.

Electrical property measurements

Fig. 8 shows the temperature dependence of the reduced electrical resistivity of the two samples Ce($Rh_{0.9}Ru_{0.1}$)Sn and Ce($Rh_{0.25}Ru_{0.75}$)Sn. (*Due to the presence of many pores and microcracks in the samples, the absolute value of* $\rho(T)$ *could not be determined accurately*; *for this reason, the reduced resistivity is reported*). Before explaining this behavior, we make reference to the electrical resistivity measurements of CeRhSn (inset of Fig. 8) [36]. For this ternary stannide, the ρ *versus* T plot was reported for a polycrystalline sample: in the first case, $\rho(T)$ decreases practically linearly with decreasing temperature from 300 to 90 – 100 K, then more rapidly at lower temperatures. The magnetic contribution ρ_m estimated by subtracting the data for LaRhSn from that of CeRhSn shows a maximum around 50 K. This behavior is characteristic of cerium intermetallics that exhibit valence instabilities. The electrical resistivity of Ce($Rh_{0.9}Ru_{0.1}$)Sn shows a behavior somehow comparable to that reported for CeRhSn: ρ decreases slowly between 280 and 50 – 60 K, and more rapidly at low temperature. Ce($Rh_{0.9}Ru_{0.1}$)Sn additionally shows a broad plateau in the temperature

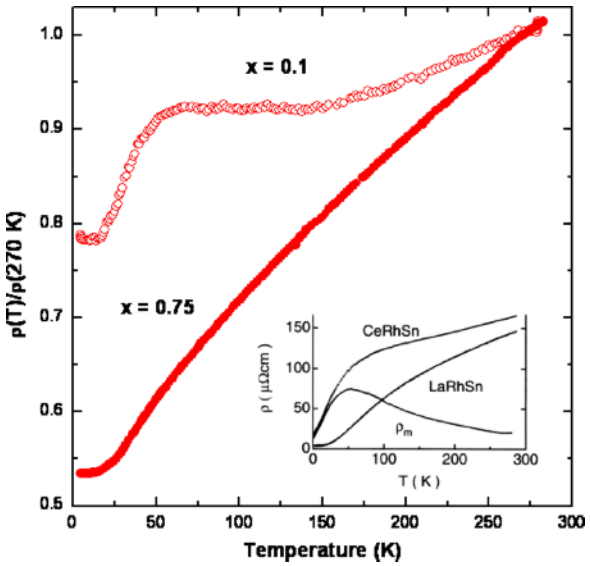

Fig. 8 (color online). Temperature dependence of the reduced electrical resistivity of $Ce(Rh_{1-x}Ru_x)Sn$ with $x = 0.1$ and 0.75. The inset presents the temperature dependence of the electrical resistivity of CeRhSn and LaRhSn and also the magnetic resistivity ρ_m of CeRhSn [34].

range around 160 K. On the contrary, the electrical resistivity of $Ce(Rh_{0.25}Ru_{0.75})Sn$ exhibits a different behavior (Fig. 8). Its curve $\rho = f(T)$ agrees with that observed for a normal metal: ρ decreases practically linearly with decreasing temperature between 280 and 25 K, and then shows a tendency to saturation. Also, it is interesting to note that the value of $\rho(T)/\rho(270\,\mathrm{K})$ determined at 4.2 K is smaller for $Ce(Rh_{0.25}Ru_{0.75})Sn$ than for $Ce(Rh_{0.9}Ru_{0.1})Sn$ indicating an increase of the metallic behavior in the solid solution following an increase of the ruthenium content.

XANES – X-ray absorption near edge structure

X-Ray absorption spectroscopy (XAS) at the CeL_{III} edge is considered a powerful tool for studying the valence state in cerium compounds. It has been particularly interesting for detecting mixed valence in several cerium-based materials since it gives a relevant representation of the electronic configuration yielding the $4f$ occupation number. In the ground state of the mixed valence compounds, the energies of Ce $4f^0$ and $4f^1$ configurations are located close to each other and mixed by the hybridization between the $4f$ and conduction band states. In the final state of the CeL_{III} XAS spectra, the energies of the two configurations are assumed to be separated by a strong core-hole potential (~10 eV) on the $4f$ state. As a consequence, the spectrum exhibits a characteristic double-peak profile that is considered as an evidence of the mixed-valence state. Thus, assuming that the L_{III} absorption is a single-particle process and neglecting final state effects, the intensity ratio of the two peaks can be used for an estimation of the averaged valence number. This procedure has been successfully applied in a wide variety of mixed valence rare earths [37 – 39].

The normalized CeL_{III} edge XANES spectrum for the CeRuSn and $Ce(Rh_{1-x}Ru_x)Sn$ solid solutions is presented in Fig. 9. All spectra show a main 'white line' at the energy of 5726 eV that can be attributed to the final state configuration of Ce^{3+}. Additionally,

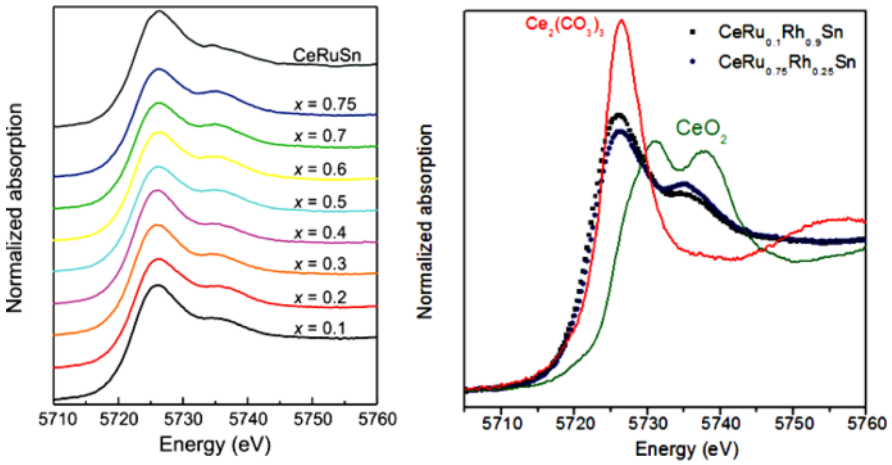

Fig. 9 (color online). Normalized L_{III} XANES spectra of a) $Ce(Rh_{1-x}Ru_x)Sn$ ($x = 0.1 - 0.75$) and CeRuSn compounds; b) $Ce(Rh_{0.9}Ru_{0.1})Sn$ and $Ce(Rh_{0.25}Ru_{0.75})Sn$ plotted together with $Ce_2(CO_3)_3$ and CeO_2 as reference compounds.

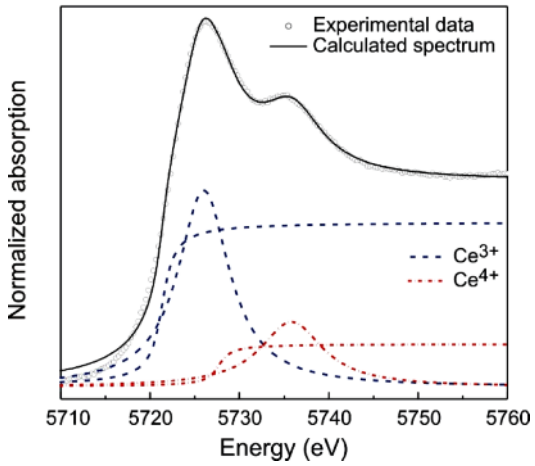

Fig. 10 (color online). Fitting of $CeRh_{0.25}Ru_{0.75}Sn$ CeL_{III} XANES spectrum with the combination of Lorentzian and arctangent functions for the Ce^{3+} and Ce^{4+} contributions.

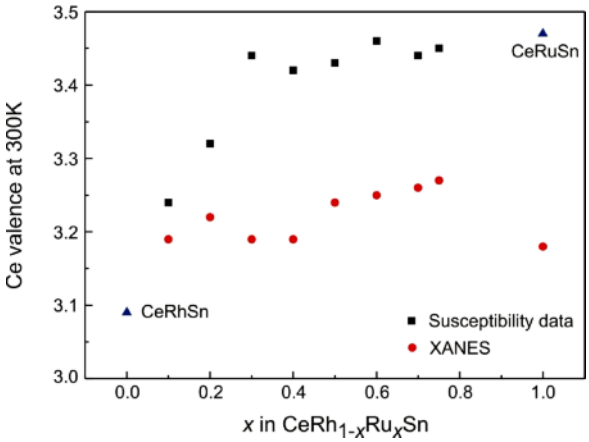

Fig. 11 (color online). Development of the cerium valence at 300 K in dependence of the ruthenium content. It contains the calculated ones at 300 K by the ICF model, literature results for CeRhSn [41] and CeRuSn [12], and values determined by XANES.

they show a shoulder at the energy of nearly 10 eV above the main white line which can be ascribed to the Ce^{4+} electronic configuration. The absorption spectra were fitted by a least-squares procedure using arctangent functions to describe the transitions into the continuum states and Lorentzian functions to take into account the $4f$ states. Because there is a high overlap of these functions, the fittings were performed by carefully varying the parameters that define the Lorentzians and arctangent functions. For each spectrum, a first fitting was performed in which the width of the arctangent and Lorentzian functions were left free. A second fit was performed with widths fixed to the average value found in the different sample fittings. The average widths values were 1 for the arctang functions and about 7.4 and 7.8 for the first and second Lorentzian functions, respectively. The energy gap between the two components was determined to be in the range of 9.6 to 10.15 eV in the different sample fittings. As an example, the deconvolution process performed for the $CeRh_{0.25}Ru_{0.75}Sn$ sample is shown in Fig. 10.

The ratio of the fractions of Ce^{4+} and Ce^{3+} ions was estimated by the ratio of the areas of the two Lorentzian curves. The values of the average valence determined for all the samples studied in the present work are reported in Table 3. Approximately, the cerium valence increases with higher ruthenium content up to $x = 0.3$, and then remains almost constant in accordance with the results of the magnetic investigations reported above. The absolute cerium valences determined by XANES are significantly smaller (3.19 – 3.27) than the ones obtained by susceptibility measurements (3.24 – 3.45) (Fig. 11). Taking into account that the cerium valence in CeO_2 determined by XANES is only about 3.5, the results of both methods are consistent [40]. The cerium valence in CeRuSn of 3.18 is equal to the value reported by Feyerherm *et al.* [15].

Table 3. Estimated average cerium valence for the stannides $Ce(Rh_{1-x}Ru_x)Sn$ and CeRuSn determined by fitting of the XANES spectra.

Compound	Average Ce valence from XANES fittings
CeRuSn	3.18(2)
$Ce(Rh_{0.9}Ru_{0.1})Sn$	3.19(2)
$Ce(Rh_{0.8}Ru_{0.2})Sn$	3.22(2)
$Ce(Rh_{0.7}Ru_{0.3})Sn$	3.19(2)
$Ce(Rh_{0.6}Ru_{0.4})Sn$	3.19(2)
$Ce(Rh_{0.5}Ru_{0.5})Sn$	3.24(2)
$Ce(Rh_{0.4}Ru_{0.6})Sn$	3.25(2)
$Ce(Rh_{0.3}Ru_{0.7})Sn$	3.26(2)
$Ce(Rh_{0.25}Ru_{0.75})Sn$	3.27(2)

^{119}Sn Mössbauer spectroscopy

Experimental and simulated ^{119}Sn Mössbauer spectra of $Ce(Rh_{1-x}Ru_x)Sn$ with $x = 0.2$, 0.5 and 0.75 at 298 K are presented in Fig. 12. Furthermore, $Ce(Rh_{0.5}Ru_{0.5})Sn$ was measured at 78 K, and the spec-

Table 4. Fitting parameters for ^{119}Sn Mössbauer spectroscopic measurements on $Ce(Rh_{1-x}Ru_x)Sn$ ($x = 0.2$, 0.5 and 0.75): temperature (T), isomer shift (δ_{iso}), electric quadrupole interaction (ΔE_Q), and experimental line width (Γ).

Compound	T (K)	δ_{iso} (mm s^{-1})	ΔE_Q (mm s^{-1})	Γ (mm s^{-1})
$Ce(Rh_{0.8}Ru_{0.2})Sn$	298	1.81(1)	0.54(1)	0.95(1)
$Ce(Rh_{0.5}Ru_{0.5})Sn$	298	1.79(1)	0.55(2)	0.93(3)
$Ce(Rh_{0.5}Ru_{0.5})Sn$	78	1.82(1)	0.57(1)	0.99(2)
$Ce(Rh_{0.25}Ru_{0.75})Sn$	298	1.80(1)	0.53(1)	0.89(2)

trum is shown in Fig. 13. All experimental data could be fitted as expected by one resonance since CeRhSn (ZrNiAl type) contains only one crystallographically independent tin site. The corresponding fitting parameters are listed in Table 4.

All samples show isomer shift values of about $\delta \approx 1.80$ mm s^{-1}. This is a typical value for intermetallic tin compounds. Mg_2Sn exhibits the same value, and Sn was assigned the valence state 0 [41]. CeRhSn also shows a comparable value of $\delta = 1.81$ mm s^{-1} at 293 K [24, 42], and the quadrupolar splittings and line widths show nearly the same values in all measurements. As expected, the non-cubic site symmetry results in small quadrupolar splittings of about $\Delta E_Q \approx 0.55$ mm s^{-1}. Line widths of about $\Gamma \approx 0.95$ mm s^{-1} can be considered good results for intermetallic stannides.

The similar isomer shifts prove that the different cerium valences are not related to the tin atoms. Because of the special bonding situation between cerium and ruthenium this results was expected. ^{99}Ru Mössbauer spectroscopy investigations are planned to clarify this unique behavior.

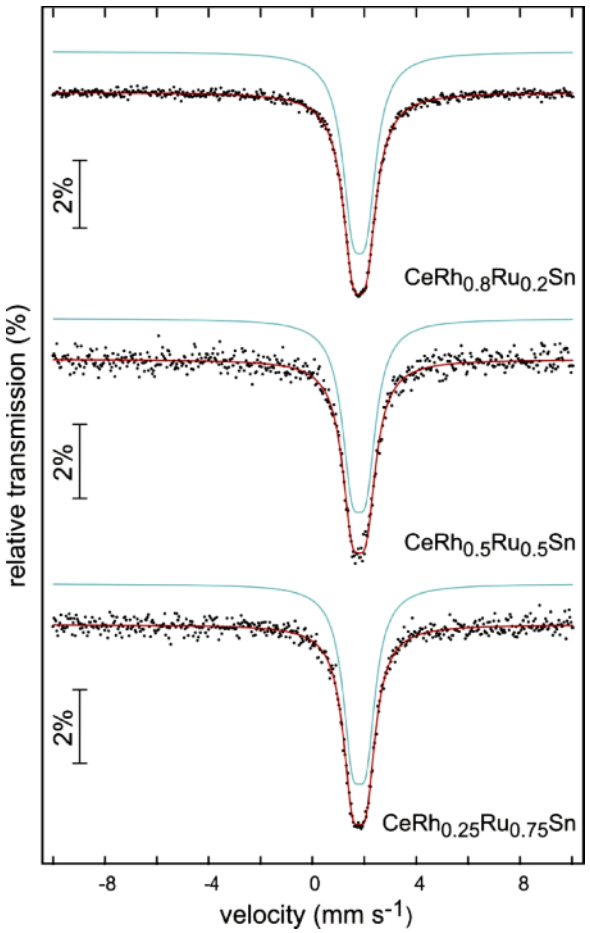

Fig. 12 (color online). Experimental and simulated ^{119}Sn Mössbauer spectra of $Ce(Rh_{1-x}Ru_x)Sn$ with $x = 0.2$, 0.5 and 0.75 at 298 K.

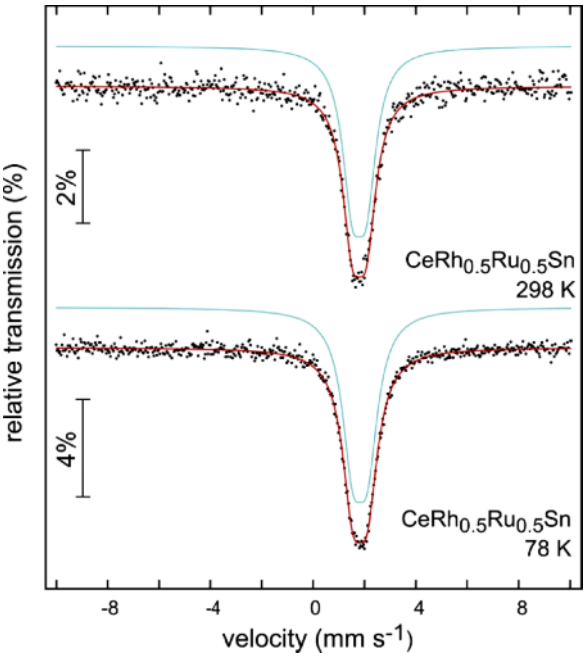

Fig. 13 (color online). Experimental and simulated ^{119}Sn Mössbauer spectra of $Ce(Rh_{0.5}Ru_{0.5})Sn$ at 298 K and 78 K.

Conclusions

The ZrNiAl-type stannide CeRhSn form a continuous solid solution $Ce(Rh_{1-x}Ru_x)Sn$ up to $x \approx 0.8$, followed by a switch to the monoclinic CeRuSn type. The samples of the solid solutions were studied by temperature-dependent magnetic susceptibility and resistivity measurements as well as by specific heat study, ^{119}Sn Mössbauer spectroscopy and XANES. All samples exhibit intermediate-valent cerium, and the data are interpreted in terms of the Sales-Wohlleben interconfiguration fluctuation (ICF) model.

Acknowledgement

This work was supported by the Deutsche Forschungsgemeinschaft. O. N. is indebted to the NRW Forschungsschule *Molecules and Materials – A common Design Principle* for a PhD fellowship.

[1] H. Fujii, Y. Uwatoko, M. Akayama, K. Satoh, Y. Maeno, T. Fujita, J. Sakurai, H. Kamimura, T. Okamoto, *Jpn. J. Appl. Phys.* **1987**, Suppl. Issue *26-3*, 549.
[2] Ch. D. Routsi, J. K. Yakinthos, H. Gamari-Seale, *J. Magn. Magn. Mater.* **1992**, *117*, 79.
[3] R. Pöttgen, H. Borrmann, R. K. Kremer, *J. Magn. Magn. Mater.* **1996**, *152*, 196.
[4] P. Rogl, B. Chevalier, M. J. Besnus, J. Etourneau, *J. Magn. Magn. Mater.* **1989**, *80*, 305.
[5] J. F. Riecken, G. Heymann, T. Soltner, R.-D. Hoffmann, H. Huppertz, D. Johrendt, R. Pöttgen, *Z. Naturforsch.* **2005**, *60b*, 821.
[6] J.-L. Bobet, M. Pasturel, B. Chevalier, *Intermetallics* **2006**, *14*, 544.
[7] B. Chevalier, A. Wattiaux, J.-L. Bobet, *J. Phys.: Condens. Matter* **2006**, *18*, 1743.
[8] G. M. Kalvius, A. Kratzer, G. Grosse, D. R. Noakes, R. Wäppling, H. von Löhneysen, T. Takabatake, Y. Echizen, *Physica B* **2000**, *289 – 290*, 256.
[9] A. Ślebarski, J. Spałek, *J. Magn. Magn. Mater.* **2007**, *310*, e209.
[10] A. Ślebarski, J. Goraus, *Phys. Stat. Sol. B* **2010**, *247*, 710.
[11] R.-D. Hoffmann, R. Pöttgen, *Z. Kristallogr.* **2001**, *216*, 127.
[12] J. F. Riecken, W. Hermes, B. Chevalier, R.-D. Hoffmann, F. M. Schappacher, R. Pöttgen, *Z. Anorg. Allg. Chem.* **2007**, *633*, 1094.
[13] S. F. Matar, J. F. Riecken, B. Chevalier, R. Pöttgen, V. Eyert, *Phys. Rev. B* **2007**, *76*, 174434.
[14] J. Mydosh, A. M. Strydom, M. Baenitz, B. Chevalier, W. Hermes, R. Pöttgen, *Phys. Rev. B* **2011**, *83*, 054411.
[15] R. Feyerherm, E. Dudzik, S. Valencia, J. A. Mydosh, Y.-K. Huang, W. Hermes, R. Pöttgen, *Phys. Rev. B* **2012**, *85*, 085120.
[16] F. M. Schappacher, P. Khuntia, A. K. Rajarajan, M. Baenitz, J. A. Mydosh, B. Chevalier, S. F. Matar, R. Pöttgen, *Z. Naturforsch.* **2012**, *67b*, 473.
[17] J. Fikáček, J. Prokleška, M. Míšek, J. Custers, S. Daniš, J. Prchal, V. Sechovský, *Phys. Rev. B* **2012**, *86*, 054108.
[18] K. Prokeš, J. Mydosh, O. Prokhnenko, W.-D. Stein, S. Landsgesell, W. Hermes, R. Feyerherm, R. Pöttgen, *Phys. Rev. B* **2013**, *87*, 094421.
[19] J. Fikáček, J. Prchal, J. Prokleška, I. Císařová, V. Sechovský, *Solid State Phen.* **2013**, *194*, 40.
[20] W. Hermes, S. F. Matar, R. Pöttgen, *Z. Naturforsch.* **2009**, *64b*, 901.
[21] T. Mishra, R.-D. Hoffmann, C. Schwickert, R. Pöttgen, *Z. Naturforsch.* **2011**, *66b*, 771.
[22] Yu.N. Grin', O. M. Sichevich, V. A. Bruskov, R. M. Rykhal', Ya. P. Yarmolyuk, *Kristallografiya* **1983**, *28*, 587.
[23] O. Niehaus, R. Pöttgen, unpublished results.
[24] T. Schmidt, D. Johrendt, C. P. Sebastian, R. Pöttgen, K. Łątka, R. Kmieć, *Z. Naturforsch.* **2005**, *60b*, 1036.
[25] Y. Echizen, K. Yamane, T. Takabatake, *Physica B* **2003**, *329 – 333*, 522.
[26] R. Pöttgen, Th. Gulden, A. Simon, *GIT Labor Fachzeitschrift* **1999**, *43*, 133.
[27] B. Chevalier, C. P. Sebastian, R. Pöttgen, *Solid State Sci.* **2006**, *8*, 1000.
[28] J. Emsley, *The Elements*, 3rd ed., Oxford University Press Oxford, **1999**.
[29] D. Kaczorowski, P. Rogl, K. Hiebl, *Phys. Rev. B* **1996**, *54*, 9891.
[30] B. C. Sales, D. K. Wohlleben, *Phys. Rev. Lett.* **1975**, *35*, 1240.
[31] B. Buffat, B. Chevalier, M. H. Tuilier, B. Lloret, J. Etourneau, *Solid State Commun.* **1986**, *59*, 17.
[32] A. Ślebarski, M. B. Maple, E. J. Freeman, C. Sirvent, M. Radłowska, A. Jezierski, E. Granado, Q. Huang, J. W. Lynn, *Phil. Mag. B* **2002**, *82*, 943.
[33] Y. Öner, V. Goruganti, O. Kamer, M. Guillot, J. H. Ross, Jr., *J. Appl. Phys.* **2008**, *103*, 07B915.
[34] M. E. Huntelaar, A. S. Booij, E. H. P. Cordfunke, R. R. van der Laan, A. C. G. van Genderen, J. C. van Miltenburg, *J. Chem. Thermodyn.* **2000**, *32*, 465.

[35] U. B. Paramanik, Anupam, U. Burkhardt, R. Prasad, C. Geibel, Z. Hossain, *J. Alloys Compd.* **2013**, *580*, 435.
[36] Y. Bando, T. Suemitsu, K. Takagi, H. Tokushima, Y. Echizen, K. Katoh, K. Umeo, Y. Maeda, T. Takabatake, *J. Alloys Compd.* **2000**, *313*, 1.
[37] A. Kotani, K. O. Kvashnina, P. Glatzel, J. C. Parlebas, G. Schmerber, *Phys. Rev. Lett.* **2012**, *108*, 036403.
[38] J. Chaboy, A. Marcelli, L. Bozukov, F. Baudelet, E. Dartyge, A. Fontaine, S. Pizzini, *Phys. Rev. B* **1995**, *51*, 9005.
[39] O. Isnard, S. Miraglia, K. H. J. Buschow, *Physica B* **1997**, *239*, 365.
[40] R. Niewa, Z. Hu, C. Grazioli, U. Rößler, M. S. Golden, M. Knupfer, J. Fink, H. Giefers, G. Wortmann, F. M. F. de Groot, F. J. DiSalvo, *J. Alloys Compd.* **2002**, *346*, 129.
[41] P. E. Lippens, *Phys. Rev. B* **1999**, *60*, 4576.
[42] K. Łatka, R. Kmieć, R. Kruk, A. W. Pacyna, M. Rams, T. Schmidt, R. Pöttgen, *Nukleonika* **2003**, *48*, S35.